



# The CO<sub>2</sub> photoconversion over reduced graphene oxide based on Ag/TiO<sub>2</sub> photocatalyst in an advanced meso-scale continuous-flow photochemical reactor

Samar Nabil<sup>1</sup> · Ahmed S. Hammad<sup>2</sup> · Haitham M. El-Bery<sup>3</sup> · Elsayed A. Shalaby<sup>1</sup> · Ahmed H. El-Shazly<sup>4,5</sup>

Received: 23 November 2020 / Accepted: 17 February 2021 / Published online: 9 March 2021  
© The Author(s), under exclusive licence to Springer-Verlag GmbH, DE part of Springer Nature 2021

## Abstract

This study aims at examining the use of an advanced meso-scale continuous-flow photochemical reactor for the photocatalytic conversion of CO<sub>2</sub> with water into fuel over TiO<sub>2</sub> (P25), Ag/TiO<sub>2</sub>, and Ag/TiO<sub>2</sub>/RGO catalysts. The silver loaded photocatalysts were prepared by one-step process via hydrothermal method. The prepared photocatalysts were characterized by various characterization techniques in order to identify the morphological, chemical, physical, and optical properties. The photocatalytic activity of the as-prepared catalysts was firstly examined by the photoelectrochemical (PEC) measurements and secondly by the photocatalytic reduction of CO<sub>2</sub> in the proposed setup. Liquid products were analyzed using gas chromatography-mass spectrometry (GC-MS) and total organic carbon (TOC) techniques. It was found that the ternary composite revealed an outstanding performance towards CO<sub>2</sub> photocatalytic reduction, where its selectivity was directed towards methanol production. The incorporation of graphene nanosheets enhanced the photocatalytic reduction of CO<sub>2</sub> by 3.3 and 9.4 times compared with Ag/TiO<sub>2</sub> and bare TiO<sub>2</sub>, respectively, using the proposed photochemical reactor in a continuous mode. This study sheds the light on a novel type of a photocatalytic reactor where CO<sub>2</sub> conversion over Ag/TiO<sub>2</sub>/RGO ternary composite was evaluated.

**Keywords** CO<sub>2</sub> photocatalytic reduction · Ag/TiO<sub>2</sub>/RGO · Ag/TiO<sub>2</sub> · Continuous mode

## Introduction

The increase of CO<sub>2</sub> concentration is the main contributor in the global warming phenomenon. Many strategies have been recently improved to eliminate carbon emissions. Carbon capture and storage (CCS) is one of the proposed technologies

used to fix CO<sub>2</sub> level. Carbon capture step could be achieved via amine scrubbing and calcium looping while storage could be done in geological formations such as deep coal seams, oil and gas reservoirs, and underground saline aquifers (Crake et al. 2017; Xiaofeng Chang and Zheng 2015; Ola and Maroto-Valer 2015). However, the use of this strategy may lead to an increase in CO<sub>2</sub> emissions due to the energy consumption via separation, purification, compression, transportation, and storage of CO<sub>2</sub> (Xiaofeng Chang and Zheng 2015; Sneddon et al. 2014; Wu et al. 2017).

Carbon capture and utilization (CCU) is an interesting technique to capture CO<sub>2</sub> then it could be converted to chemical feedstock which means utilization of CO<sub>2</sub>. Conversion of CO<sub>2</sub> could be carried out chemically, electrochemically, or photoelectrochemically to produce various hydrocarbons (Low et al. 2017; Wang et al. 2018; Karamian and Sharifnia 2016). Among those techniques, the photocatalytic reduction of CO<sub>2</sub> is the most promising approach that employs an infinite energy source which is solar energy to produce different valuable hydrocarbons (Low et al. 2017; Chang et al. 2016).

The photoreactor design is the most important factor influencing the efficiency of the photoreduction of CO<sub>2</sub> and

Responsible Editor: Ricardo Torres-Palma

✉ Samar Nabil  
samar.nabil@alexu.edu.eg

<sup>1</sup> Department of Environmental Studies, Institute of Graduate Studies and Research, Alexandria University, Alexandria 21526, Egypt

<sup>2</sup> Chemical Engineering Department, Faculty of Engineering, Port Said University, Port Said, Egypt

<sup>3</sup> Advanced Functional Materials Laboratory, Chemistry Department, Faculty of Science, Assiut University, Assiut 71515, Egypt

<sup>4</sup> Chemical and Petrochemicals Engineering Department, Egypt-Japan University of Science and Technology, Alexandria 21934, Egypt

<sup>5</sup> Chemical Engineering Department, Faculty of Engineering, Alexandria University, Alexandria 21544, Egypt

the product yield rates (M. Tahir and Amin 2013) (Tahir et al. 2015). An efficient photoreactor should include the following: (1) high (active catalyst surface area: reactor volume) ratio, (2) uniform distribution of light and its utilization, (3) superior photonic efficiency, and (4) high throughput with lower power consumption (B. Tahir et al. 2015).

Several types of reactors were used for CO<sub>2</sub> photoconversion over the last decades such as follows: slurry, fluidized, and fixed bed reactors. Some drawbacks were reported using these reactors such as follows: inefficient light distribution, fewer catalyst recycling possibilities, product separation challenges especially with slurry reactors, and lower surface to volume ratio in case of fixed bed reactors.

Later, optical fiber photoreactors have been investigated for CO<sub>2</sub> photoreduction. These reactors offer a uniform and efficient light to the photocatalyst surface, thus increases the efficiency of photon-conversion process. However, the optical fiber configuration cannot effectively utilize the entire reactor volume (Tahir and Amin 2013; Tahir et al. 2015). Besides, when a bundle of optical fibers is coated, fragility of the optical fibers and the durability of coatings have been described as disadvantages associated with their usage. Also, heat accumulation from a bundle of fibers may lead to deactivation of catalyst. As a result, these limitations prevent the commercial usage of the reactor (Ola and Maroto-Valer 2015).

Recently, the commonly used reactor is the monolith. It has many benefits such as the high surface to volume ratio, probability of scaling up through increasing its dimensions and channels, and controlling its structural parameters (i.e., pore-volume, pore size and surface area) (Ola and Maroto-Valer 2015). However, the main disadvantage of the monolith structure is the light distribution hindered through interconnected channels of the monolith. Moreover, the deactivation of the immobilized catalyst with continuous flow conditions also limits its use in the industry.

Tahir et al. (2015) investigated the use of monolith reactor in CO<sub>2</sub> photoreduction by H<sub>2</sub> in both batch and continuous modes. They found that CH<sub>4</sub> was the main product in the batch system; however, CO is the main one in case of continuous mode. They attributed the production of CH<sub>4</sub> in the batch process to the accumulation of products in the reaction chamber with irradiation time while in a continuous system, the continual feeding and products removal led to lower yield rates through the production of CO. Moreover, in the continuous process, they described that the catalyst partially lost its photoactivity within 4 h of irradiation time and almost deactivated after 6 h of irradiation time.

Currently, the use of the microchannel reactors provides many benefits due to their ability to be operated continuously as well as offering the option of utilizing light-emitting diodes (LED) lamps which provides extra advantage for energy saving (Heggo et al. 2016). Also, their avoidance of the previously reported limitations and drawbacks of other reactors

increases their usage in many photocatalytic applications. However, most studies mentioned their usage on a lab-scale with small production quantities which could control their scale-up in the industrial processes (Loubière et al. 2016).

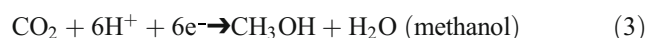
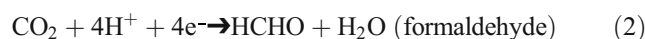
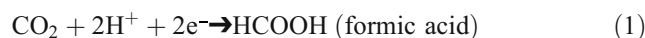
Thus, there is an urgent need for developing the photocatalytic reactors to meet the industrial scaling up. Besides, the design of the photochemical reactors operated in a continuous mode considers the driving force to develop more photochemical reactors.

In this study, we investigated our setup with an advanced meso-scale continuous-flow-type photochemical reactor which provides the following advantages (Josland et al. 2016): (1) continuous flow processing, (2) relatively higher production quantities comparing with other types of reactors (several grams per day) which increases the probability of the industrial scaling up (Loubière et al. 2016), (3) inner irradiation, (4) uniform light distribution, (5) lower power consumption due to the use of LED lamp, and (6) high surface area to volume ratio which enhances both photon and mass transfer (Loubière et al. 2016; Némethné-Sóvágó and Benke 2014). Moreover, it is well known that the solubility of CO<sub>2</sub> increases with decreasing the temperature so that we introduce a cooling water bath with a continuous flow of CO<sub>2</sub> gas into water to overcome the low solubility of CO<sub>2</sub> with water.

The integration of the photochemical reactor with the proposed setup provides the opportunity to feed fresh catalyst particles suspended in water saturated with CO<sub>2</sub> to be entered to the reactor by each minute simultaneously with the collection of gaseous and liquid products. Thus, there is no option for catalyst deactivation as in the other kinds of photoreactors used in CO<sub>2</sub> reduction.

Many previous studies reported the importance of graphene use in their applications (Wei et al. 2017; Zang et al. 2017; Liu et al. 2018). In order to further improve the photoconversion of CO<sub>2</sub>, RGO was incorporated with Ag/TiO<sub>2</sub> (Akhavan and Ghaderi 2009) to prepare the ternary nanocomposite of Ag/TiO<sub>2</sub>/RGO. The superior electrical conductivity of RGO facilitates the separation of photogenerated charges which consequently enhanced the CO<sub>2</sub> reduction.

The kind of CO<sub>2</sub> photocatalytic reduction products depends mainly on the number of electrons formed from the semiconductor used in the system. Thus, the expected products of CO<sub>2</sub> reduction could be formic acid and/or formaldehyde and/or methanol which could be illustrated by the following equations (Habisreutinger et al. 2013; Chang et al. 2016):



Our proposed setup together with the synthesized catalysts exhibited an outstanding performance towards CO<sub>2</sub> photocatalytic reduction as the major product was methanol while the minor one was formaldehyde. Moreover, we have found that the amount of formed formaldehyde is too small compared to previous studies, which represents only 1.8% from the TOC.

The production of methanol has a great interest as it is easy to handle and used as an additive in gasoline and it could be converted to other useful chemicals by classic technologies (Sellaro et al. 2016). It was also reported that methanol could be used for the internal combustion engines as a source of energy by (Verhelst et al. 2019). Furthermore, it was reported by Abrishamkar and Barootkoob (2017) that formaldehyde was used as a fuel source in fuel cells.

## Experimental section

### Materials

TiO<sub>2</sub> (P25) and the metal precursor of Ag (AgNO<sub>3</sub>) were purchased from (ACROS) organics company. Graphite powder and sodium sulfate (Na<sub>2</sub>SO<sub>4</sub>) were obtained from Fisher scientific, UK. All other chemicals such as iodine (99.99%) and potassium permanganate (KMnO<sub>4</sub>) were analytical grade and commercially available.

Nitric acid (HNO<sub>3</sub>) was obtained from Merck, Germany. Both of hydrochloric acid (HCl), hydrogen peroxide (H<sub>2</sub>O<sub>2</sub>) and sulfuric acid (H<sub>2</sub>SO<sub>4</sub>) were obtained from Sigma-Aldrich while both acetone (C<sub>3</sub>H<sub>6</sub>O) and ethanol (C<sub>2</sub>H<sub>5</sub>OH) were purchased from Fisher scientific, UK. All solvents were (HPLC) grade.

### Samples preparation

Graphite oxide (GO) was firstly prepared then the exfoliated GO was further utilized and loaded with (TiO<sub>2</sub>) and metal nanoparticles (Ag) following the one-step approach of the hydrothermal method.

The conversion of graphite powder into (GO) was done using the modified Hummers' method. As shown in Fig. 1 (Li et al. 2014), graphite powder was firstly oxidized by nitric

acid (HNO<sub>3</sub>); later, the oxidizing by the slow addition of sulfuric acid (H<sub>2</sub>SO<sub>4</sub>) was also accomplished in a vessel immersed in an ice bath under stirring and sonication. Secondly, potassium permanganate (KMnO<sub>4</sub>) was added gradually to continue the oxidation process. The temperature was adjusted below 20 °C using the ice bath to avoid the temperature increase during the exothermic reaction. The mixture was further left for 24 h under continuous stirring to complete the oxidation process. In order to stop the reaction, hydrogen peroxide was added until a yellow-brown cake of (GO) was obtained then washed with HCl and distilled water for several times by decantation.

The further synthesis of the binary (Ag/TiO<sub>2</sub>) and ternary (Ag/TiO<sub>2</sub>/RGO) composites were accomplished via hydrothermal method as follows. Firstly, both TiO<sub>2</sub> suspended in water-ethanol (2:1) mixture and metal precursor of silver salt (AgNO<sub>3</sub>) were mixed under sonication and vigorous stirring to prepare (Ag/TiO<sub>2</sub>) composite. While, in case of the ternary composite (Ag/TiO<sub>2</sub>/RGO), the desired amount of GO (in this case, 5% of the total weight percentage of the composite) was firstly exfoliated in dist. H<sub>2</sub>O via ultrasonication till stable, suspension was formed. Then, GO solution was mixed with both the (AgNO<sub>3</sub>) solution and TiO<sub>2</sub> suspension under sonication and vigorous stirring in water-ethanol (2:1) mixture. The obtained mixture was then transferred to a Teflon-lined autoclave and kept for 12 h at 200°C. Finally, the resulted powder was washed several times with dist. H<sub>2</sub>O and dried at 80 °C for 24 h.

### Characterization of the as-prepared photocatalysts

The as-prepared nanocomposites were characterized firstly by a field-emission transmission electron microscope (FE-TEM) (JEOL JEM-2100F) to identify the shape, distribution, size, and surface morphology of the photocatalysts.

Then, further characterization of the morphology of the as-prepared composites was accomplished by the high-angle annular dark-field scanning transmission electron microscopy (HAADF-STEM) on a (JEOL JEM-2100F) TEM/STEM with a spherical aberration corrector.

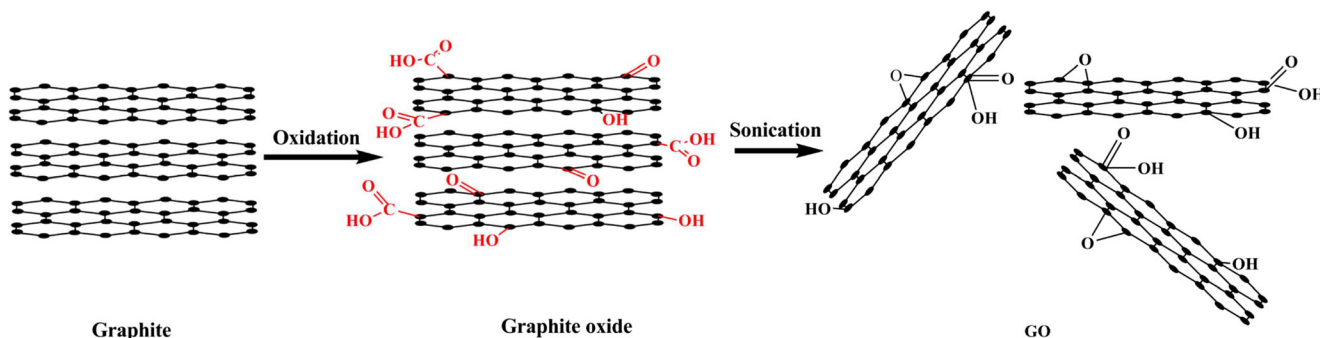


Fig. 1 Schematic of GO synthesis. Copyright (Li et al. 2014)

Moreover, the elemental analysis and the weight percentage of the samples, EDX, were accomplished by energy-dispersive X-ray spectroscopy (JEOL JEM-2100F).

Also, the phase and crystalline composition of the synthesized photocatalysts were studied by XRD pattern. The samples were firstly grounded harshly into powder prior to be analyzed. An X-ray diffractor (XRD-6100 Shimadzu, Japan) equipped with a Cu-K $\alpha$  radiation source with  $\lambda = 1.55 \text{ \AA}$  was utilized to scan the 2theta in the range of  $5^\circ$  to  $80^\circ$  at a scanning pitch of  $0.02^\circ$ .

Fourier transform infrared spectroscopy (FTIR) was performed to identify the functional groups existed in each photocatalyst. The FTIR relies on the IR-spectrum of absorption or transmission of samples. A Vertex 70 IR spectrometer (Bruker Scientific Instruments, Germany) was employed.

The Brunauer-Emmett-Teller (BET) was performed to study the specific surface area and pore size distribution. The N<sub>2</sub> adsorption/desorption isotherms were studied for the as-prepared nanocomposites. Brunauer-Emmett-Teller (BET) specific surface areas of the photocatalysts were obtained using Belsorp-mini II (BEL JAPAN) nitrogen adsorption instrument at 77 K. The powders were degassed prior to surface area analysis at  $300^\circ\text{C}$  for 3 h under vacuum.

Diffuse reflectance spectra were performed by UV-vis (Thermo Scientific, Evolution 220 coupled with ISA-220 integrated sphere). The calculations of the absorbance were obtained from reflectance data via Kubelka-Munk function.

Photoelectrochemical (PEC) measurements were performed using a potentiostat (Gamry instrument, reference 3000) in one compartment cell with a Pyrex window filled with 0.1 M Na<sub>2</sub>SO<sub>4</sub> electrolyte. Three electrodes were utilized where the platinum rod and saturated Ag/AgCl were worked as the counter electrode (C.E) and the reference electrode (R.E), respectively. Meanwhile, the third electrode was the working electrode (W.E) fabricated from different photocatalysts powder deposited via electrophoretic deposition method (EPD) of on the surface of fluorine-doped tin oxide (FTO) glass. The light irradiation source of (Suruga Seiki-Co, Japan) UV LED lamp with a wavelength of 365 nm and intensity up to  $50 \text{ mW/cm}^2$  was utilized. The weight and the coated area of each working electrode after the deposition of several catalysts on the surface of FTO glass were ca. 4 mg and ca.  $6 \text{ cm}^2$ , respectively.

## Photocatalytic reduction of carbon dioxide with water

A continuous-flow photochemical reactor system (Vapourtec UV-150) was used for CO<sub>2</sub> photoconversion into valuable organic compounds in the presence of water and light as shown in Fig. 2.

Prior to each run, the desired amount of catalyst powder was dispersed in a 65-ml distilled water bottle using ultrasonication. Then, the water bottle including the dispersed

catalyst was immersed in a water bath connected to a chiller to maintain the temperature at  $5^\circ\text{C}$  to further ensure an efficient solubility of CO<sub>2</sub> in the distilled water. The CO<sub>2</sub> bubbling was performed 30 min before starting the run with a flow rate of 35 ml/min to ensure the saturation of the CO<sub>2</sub> in the distilled water. Moreover, the continuous bubbling of CO<sub>2</sub> was utilized while the reaction proceeds to confirm a constant concentration of soluble CO<sub>2</sub> in water.

In order to begin the photocatalytic reduction of CO<sub>2</sub>, the reactor was turned on to allow feeding of suspension catalyst in liquid water saturated with CO<sub>2</sub> and the light illumination. The reaction was performed under UV light-emitting diode (LED) lamp with a wavelength of 365 nm to save energy and the liquid pump was adjusted at 500  $\mu\text{l/min}$ . The resulted products were divided into gaseous and liquid.

The gaseous products were collected in a gas bag purchased from (GL Sciences Inc., Japan) using He gas as a carrier then analyzed using gas chromatography (GC) (Shimadzu 2014, Japan) equipped with ShinCarbon ST micropacked column (Restek, length 2 m  $\times$  ID 2mm, USA) and a thermal conductivity detector (TCD). The results revealed that there was no CO or CH<sub>4</sub> found in the gas bag. Moreover, there was no H<sub>2</sub> gas detected by the GC which indicates that its amount was too small to be detected or it may be completely consumed in the reaction.

Also, the use of the previously mentioned water bath allows the resulted organic vapors in the gaseous products to be condensed in the liquid phase prior to be analyzed by GC and total organic carbon (TOC) instruments.

Firstly, the liquid products were qualitatively analyzed using GC/mass spectroscopy (MS) (Thermo-Scientific with TG-5MS capillary column [length 30m, ID 0.25mm]) after filtration and extraction. Secondly, the resulted liquid samples at the end of each run were quantitatively analyzed using total organic carbon analyzer (Shimadzu, TOC-L series, Japan) (Yang et al. 2011; Chen et al. 2012; Dong et al. 2017) and the Nash method (Nash 1953) (Shehzad et al. 2018; Kometani et al. 2017) was further used to determine the formaldehyde concentration at an absorbance wavelength of 414 nm. Blank experiments were performed and neither TOC nor formaldehyde was detected.

## Results and discussion

### Catalysts characterization

Figure 3 shows the morphology of both the TiO<sub>2</sub> (P25) and the as-prepared catalysts with TEM, HAADF-STEM images. In addition, Fig. 4 depicts the elemental mapping images as well as EDX images for Ag/TiO<sub>2</sub> and Ag/TiO<sub>2</sub>/RGO photocatalysts.

As shown in Fig. 3a, the TiO<sub>2</sub> P25 nanoparticles are spherical in shape and their particle size is ranging from 14.04

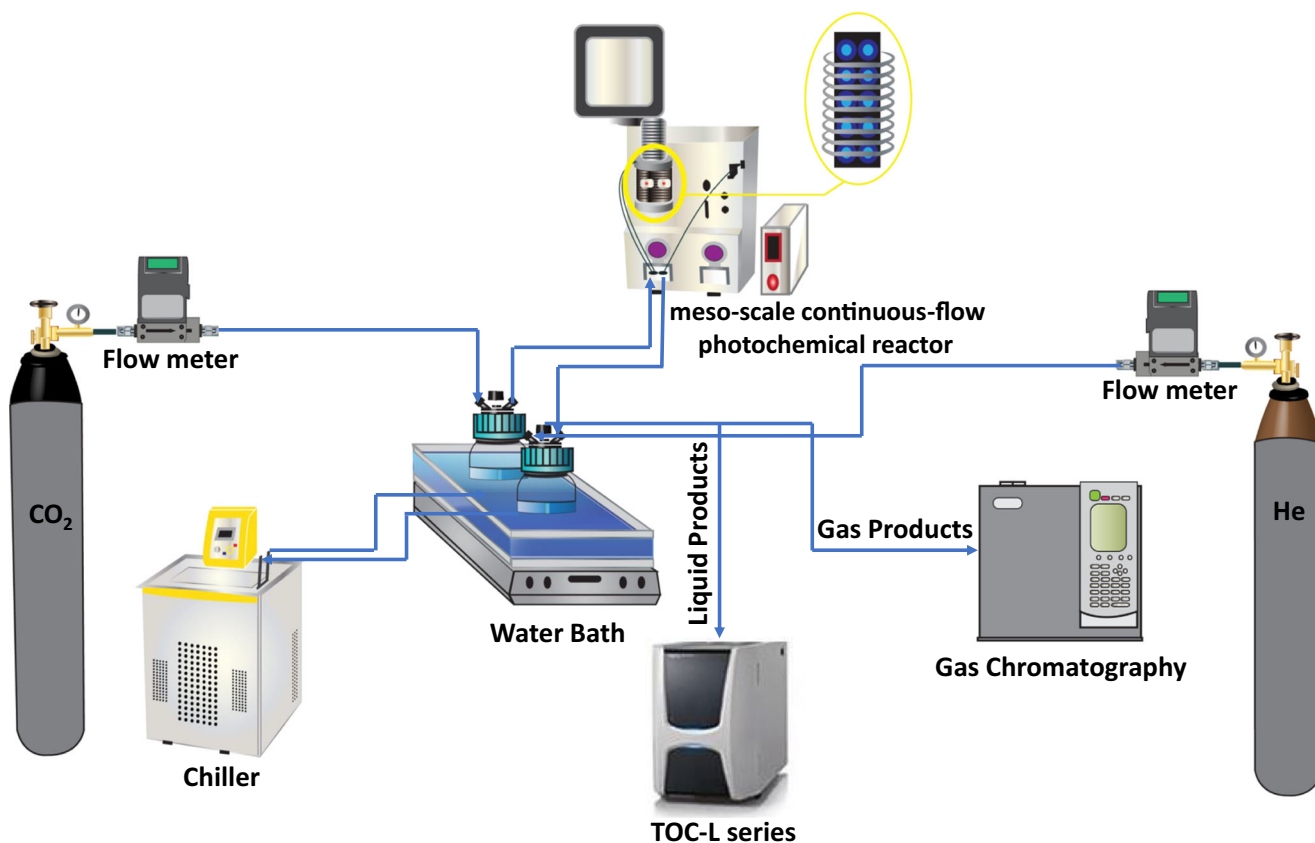


Fig. 2 Schematic diagram of the experimental setup

26.78 nm. Figure 3d shows the lattice fringes of TiO<sub>2</sub> P25 with a spacing of 0.35 nm which is corresponding to the anatase phase (101) of TiO<sub>2</sub>.

The shiny spots seen in the HAADF-STEM images appeared in Fig. 3e represent the Ag NPs. Figure 3c and e as well as Ag EDX mapping images in Fig. 4a show the uniform dispersion of Ag NPs on the surface of TiO<sub>2</sub> P25 in the as-prepared 2 wt.% Ag/TiO<sub>2</sub> catalyst. The particle size of Ag NPs was measured by TEM which is ranging from 1.33 to 4.04 nm.

Figure 3 (d, f) and 4b present the distribution of Ag NPs and RGO sheets using TEM and HAADF-STEM, and EDX mapping images respectively in the 2 wt.% Ag/TiO<sub>2</sub>/RGO ternary composite that confirm the homogenous dispersion of both elements on the surface of TiO<sub>2</sub> P25.

Moreover, EDX and EDX mapping were further used to predict the presence of Ti, O, Ag, and C elements in the as-prepared catalysts and the weight percentage of each element. It is well known that Ti and O have come from TiO<sub>2</sub> while C was originated from RGO sheets and the existence of Ag peaks confirms the presence of Ag NPs. The actual loading amounts with the weight percentage of each element in all catalysts are illustrated in Table 1.

The phase composition of all catalysts was examined by XRD pattern and the results are exhibited in Fig. 5. All peaks

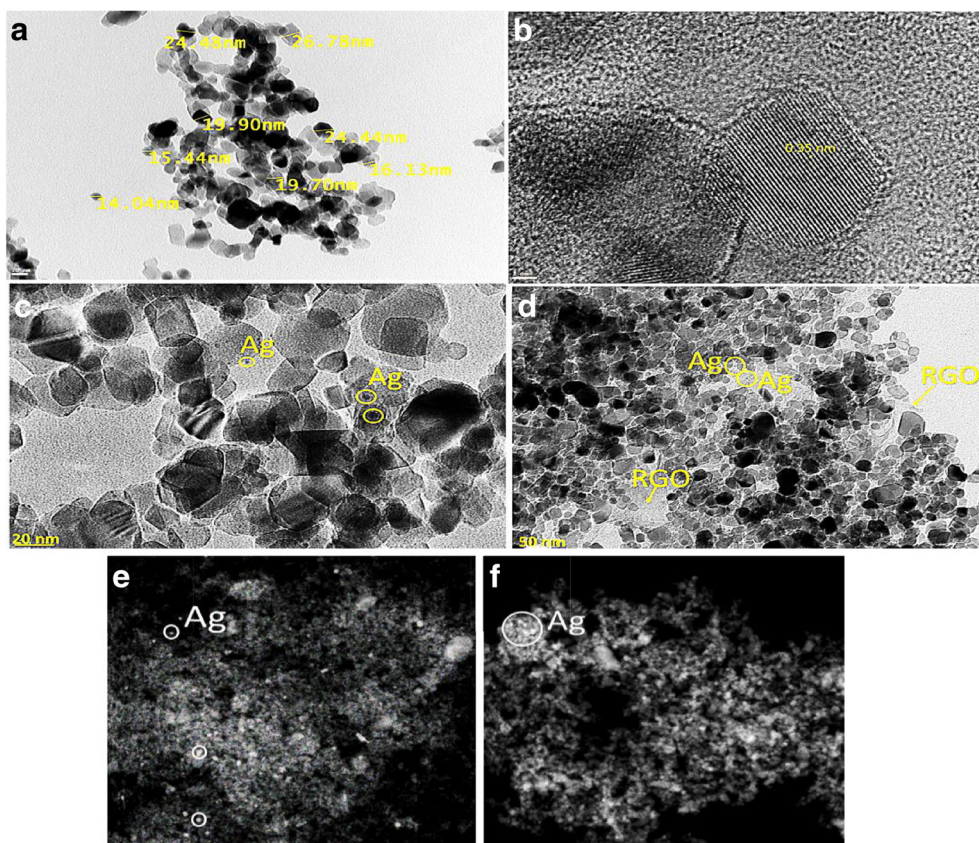
were compared with the Joint Committee on Powder Diffraction Standards (JCPDS) Card File no. 00-002-0387 and Card File no. 00-001-1292 for both tetragonal anatase and tetragonal rutile phases of TiO<sub>2</sub>, respectively. The crystal facets of the anatase phase of TiO<sub>2</sub> were (101), (103), (004), (200), (105), (211), (204), (116), (220), and (215) which are assigned to the characteristic peaks at  $2\theta = 25.18^\circ$ ,  $37.72^\circ$ ,  $38.42^\circ$ ,  $47.95^\circ$ ,  $53.90^\circ$ ,  $54.26^\circ$ ,  $62.60^\circ$ ,  $68.73^\circ$ ,  $70.14^\circ$ , and  $74.99^\circ$  of the anatase phase, respectively. While the crystal facets of the rutile phase of TiO<sub>2</sub> were (110), (101), (200), (111), and (211) which corresponding to the characteristic peaks of rutile phase appears at  $2\theta = 27.32^\circ$ ,  $36.82^\circ$ ,  $38.82^\circ$ ,  $41.18^\circ$ , and  $55.90^\circ$ , respectively. The characteristic diffraction peaks of TiO<sub>2</sub> did not change after Ag NPs loaded on the surface of TiO<sub>2</sub> and there were no significant diffraction peaks for Ag NPs as their loading was too small to be detected with XRD detection limit.

Scherrer's equation was used to calculate the average crystallite size of the synthesized catalysts according to the maximum three peaks of anatase and rutile phases.

$$L = K \lambda / \beta \cos\theta \quad (4)$$

where L is the crystallite size (nm), K is a constant depending on the crystallite shape (0.9 in this case),  $\lambda$  is the X-ray

**Fig. 3** **a** and **b** are TEM and HRTEM images of TiO<sub>2</sub> P25. **c** and **d** are TEM images of 2 wt.% Ag/TiO<sub>2</sub> with 20-nm magnification and for 2 wt.% Ag/TiO<sub>2</sub>/RGO with 50-nm magnification scale, respectively, while HAADF-STEM images of 2 wt.% Ag/TiO<sub>2</sub> and 2 wt.% Ag/TiO<sub>2</sub>/RGO are illustrated in images **e** and **f**, respectively



wavelength (nm),  $\beta$  is the full width at half maximum (FWHM), and  $\theta$  is the Bragg's angle.

The phase composition of samples was calculated using relative peak intensity of anatase and rutile (Spurr and Myers 1957) (Rajalakshmi et al. 2012).

$$F_A = 1/[1 + 1.26 (I_R/I_A)] \quad (5)$$

where  $F_A$  is the fraction of anatase phase and  $I_R$  and  $I_A$  are the intensity of the rutile (110) and anatase (101) diffraction peaks, respectively. The calculated crystallite size and phase composition for both anatase and rutile phases of all catalysts are summarized in Table 1.

As illustrated from Table 1, the percentage of rutile phase was slightly increased after the addition of Ag NPs and RGO sheets which could be assigned to temperature elevation in the hydrothermal reaction during the preparation of catalysts. The anatase to rutile transformation was also observed in previous reports during the introduction of both Ag nanoparticles and RGO sheets (Liu et al. 2017; Feng et al. 2020).

Furthermore, the crystallite size was also improved after the addition of Ag and RGO sheets which indicates the good crystallization of the as-prepared catalysts that was in consistent with the results reported by Feng et al. (2020) and Gui et al. (2015).

The examination of the functional groups and the chemical composition were performed using FTIR. Here are the FTIR spectra as exhibited in Fig. 5.

Figure 6 shows the FTIR measurements of TiO<sub>2</sub>, 2 wt.% Ag/TiO<sub>2</sub>, 2 wt.% Ag/TiO<sub>2</sub>/RGO, and GO. In case of GO spectrum, there are some characteristic peaks located at 1395, 1630, 1730, and 3400 cm<sup>-1</sup> which belong to the stretching vibrations of O=C-O carboxyl, C=C skeleton of GO or -OH water, C=O carboxylates or ketones, and -OH water, respectively (Vasilaki et al. 2015; Y. Wang et al. 2019; M. Tahir and Amin 2017). The other functional groups are located at 1075 cm<sup>-1</sup> which is assigned to C-O group of epoxy or alkoxy whereas 1250 cm<sup>-1</sup> is related to the C-O-C group of epoxide or C-O-H group of phenolic. The peaks located below 1000 cm<sup>-1</sup> are attributed to vibration of Ti-O-Ti and Ti-O-C groups. The formation of Ti-O-C absorption band confirms the reaction between TiO<sub>2</sub> NPs and GO sheets. Moreover, comparing GO and Ag/TiO<sub>2</sub>/RGO samples, the decreased intensities of oxygen absorption bands in 2 wt.% Ag/TiO<sub>2</sub>/RGO compared to GO is further proved the reduction of GO and the formation of RGO during the hydrothermal preparation reaction. This result is consistent with the previous studies (Wang et al. 2019).

To analyze the structure of all samples, Raman spectroscopy was utilized and the spectra of photocatalysts are depicted in Fig. 7. For TiO<sub>2</sub> photocatalyst, the most characteristic peak

**Fig. 4** EDX mapping and EDX images of **(a)** 2 wt% Ag/TiO<sub>2</sub> and **(b)** 2 wt% Ag/TiO<sub>2</sub>/RGO, respectively

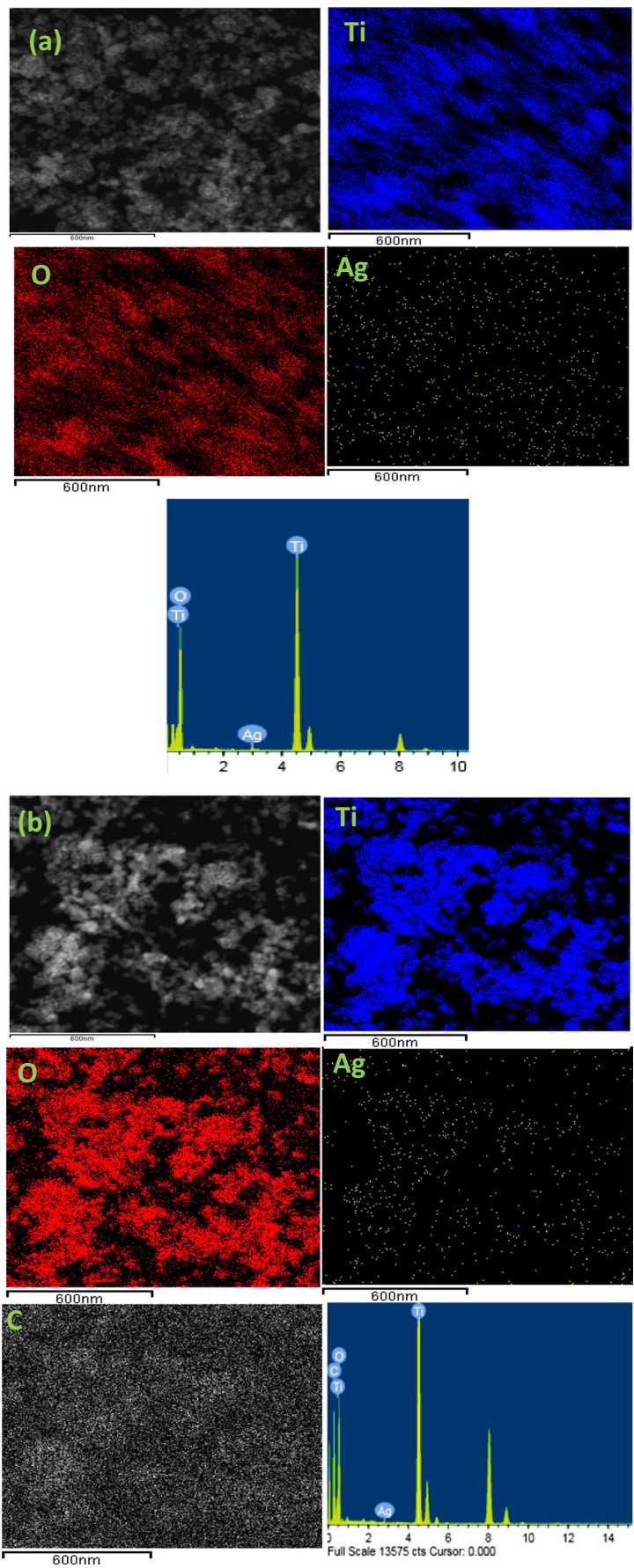


**Table 1** The EDX and XRD analysis of all catalysts

Sample	EDX analysis (wt.%)				XRD analysis		
	Ti	O	Ag	C	Phases	% of each phase	Crystallite size (nm)
TiO <sub>2</sub>	62.64	37.36	0	0	Anatase	77	15.1
					Rutile	23	18.3
2 wt.% Ag/TiO <sub>2</sub>	61.50	36.42	2.08	0	Anatase	75	15.15
					Rutile	25	19.5
2 wt.% Ag/TiO <sub>2</sub> /RGO	46.89	27.85	1.50	23.76	Anatase	70	17.5
					Rutile	30	25.3

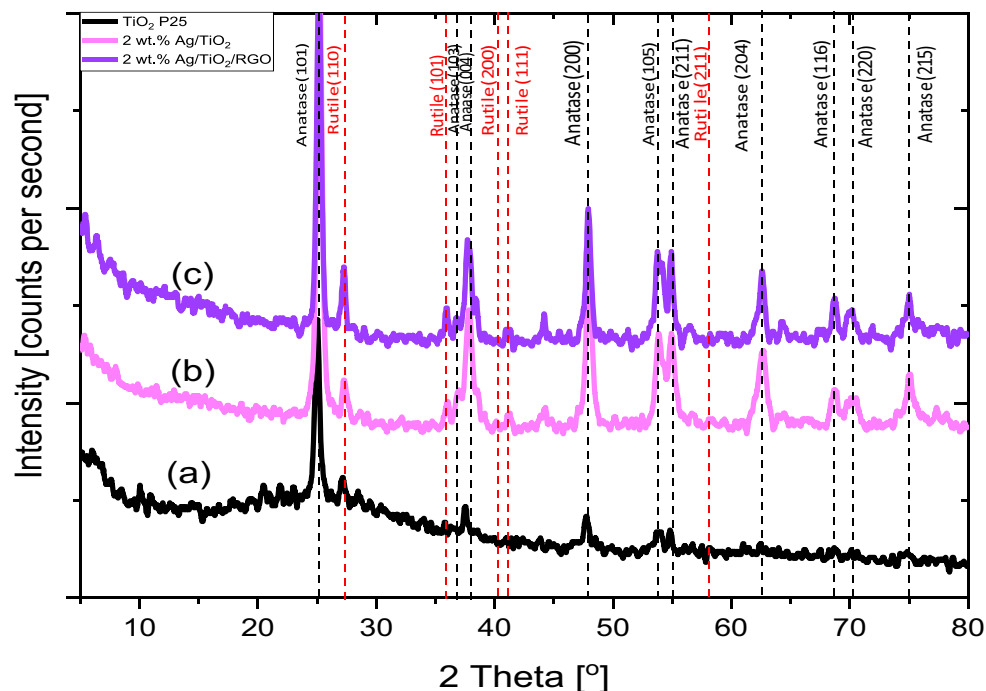
of TiO<sub>2</sub> was observed at 144 cm<sup>-1</sup> which ascribed to E<sub>g</sub> mode, while peaks at 396, 516, and 638 cm<sup>-1</sup> are corresponding to B<sub>1g</sub>, A<sub>1g</sub>, and E<sub>g</sub> modes, respectively, arising from the presence of Ti-O bond in anatase phase of TiO<sub>2</sub> (Wang et al. 2019; Naraginti and Yong 2019). The distinctive bands of GO and RGO were noticed at 1346 and 1593 cm<sup>-1</sup> for D and G bands. D band is due to graphene-disordered structure corresponding to A<sub>1g</sub> mode while G band assigns to E<sub>2g</sub> mode from C-C bond in all hybridized carbon materials sp<sup>2</sup>. In Ag/TiO<sub>2</sub> catalyst, it is well obvious that the intensities of the four characteristic peaks of TiO<sub>2</sub> were increased compared with TiO<sub>2</sub> which could be attributed to SPR effect of Ag NPs (Saquib et al. 2020).

While both the D and G bands associated to RGO along with TiO<sub>2</sub> characteristic peaks were clearly detected in the Raman spectra of Ag/TiO<sub>2</sub>/RGO nanocomposite, however, the intensities of TiO<sub>2</sub> peaks in that composite were decreased

due to the incorporation of RGO. Comparing the I<sub>D</sub>/I<sub>G</sub> ratio of the Ag/TiO<sub>2</sub>/RGO ternary composite with GO, it was noticed that the ratio was 0.68 in GO while in the ternary composite was 0.75. The increment of I<sub>D</sub>/I<sub>G</sub> ratio in the ternary composite may assigned to the increase of the defects due to the addition of Ag and TiO<sub>2</sub> NPs over graphene nanosheets as well as the reduction of the average size of sp<sup>2</sup> domains owing to the use of hydrothermal reduction of GO in which the breaking of the GO layers and the formation of multilayers edges of graphene resulting in the increase of defects (Vasilaki et al. 2015; Wang et al. 2013).

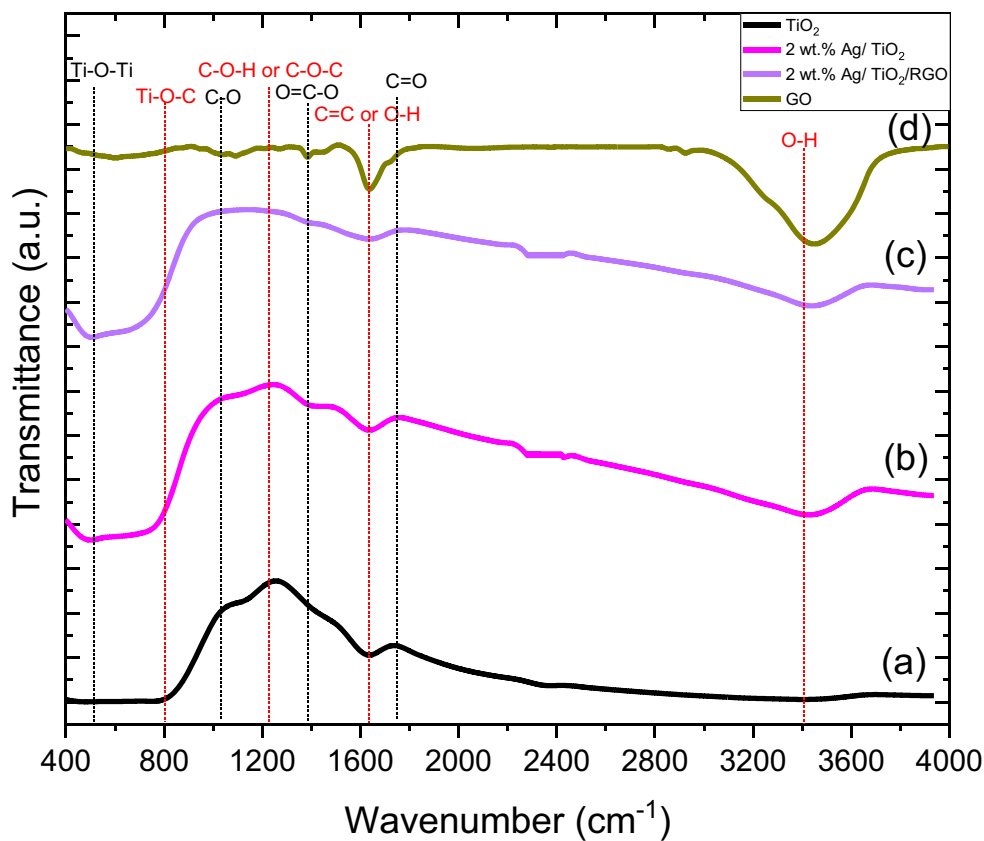
In order to determine the surface area and pore volume for the synthesized catalysts, Brunauer-Emmett-Teller (BET) and Barrett-Joyner-Halendra (BJH) methods were performed, and results are depicted in Fig. 8.

As shown in Fig. 8a, the addition of Ag NPs and RGO increases the hysteresis loops which consequently increase

**Fig. 5** XRD patterns for (a) TiO<sub>2</sub> P25, (b) 2 wt.% Ag/TiO<sub>2</sub> P25, and (c) 2 wt.% Ag/TiO<sub>2</sub> P25/RGO



**Fig. 6** FTIR for (a) TiO<sub>2</sub>, (b) 2 wt.% Ag/TiO<sub>2</sub>, (c) 2 wt.% Ag/TiO<sub>2</sub>/RGO, and (d) GO



the amount of N<sub>2</sub> adsorbed by photocatalysts. In Table 2, the surface area and pore volume of all catalysts were exhibited. It is well noticed that the incorporation of Ag and RGO positively affected both specific surface and pore volume which attributed to the improvement of the meso-porosity. These results are consistent with previous studies (Tahir and Amin

2017; (Kočí et al. 2010). All samples are IV adsorption-desorption isotherms which is corresponding to mesoporous materials with H1 hysteresis loops.

The optical properties were analyzed in the wavelength range of 200–800 nm by UV-Vis diffuse reflectance spectra (DRS). Figure 9 shows the UV-Vis diffuse reflectance spectra

**Fig. 7** Raman spectra of (a) TiO<sub>2</sub>, (b) 2 wt.% Ag/TiO<sub>2</sub>, (c) 2 wt.% Ag/TiO<sub>2</sub>/RGO, and (d) GO

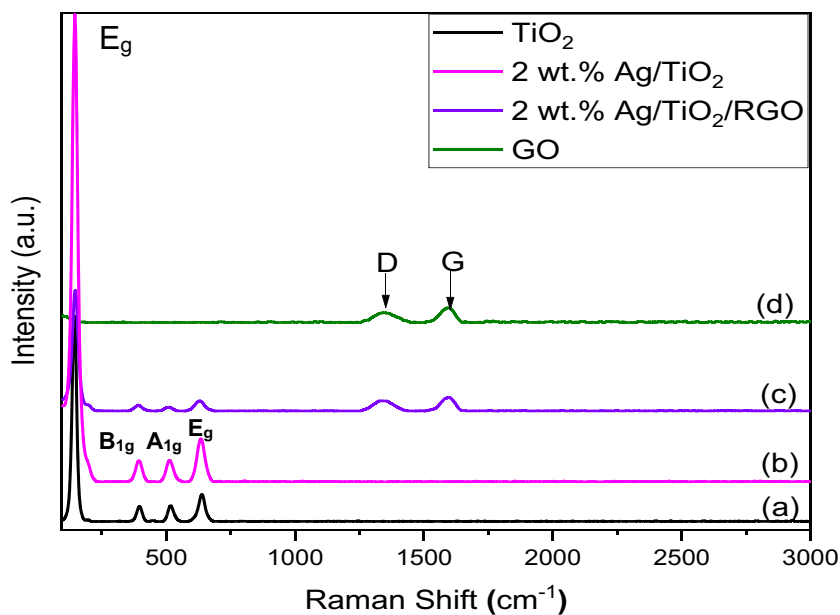
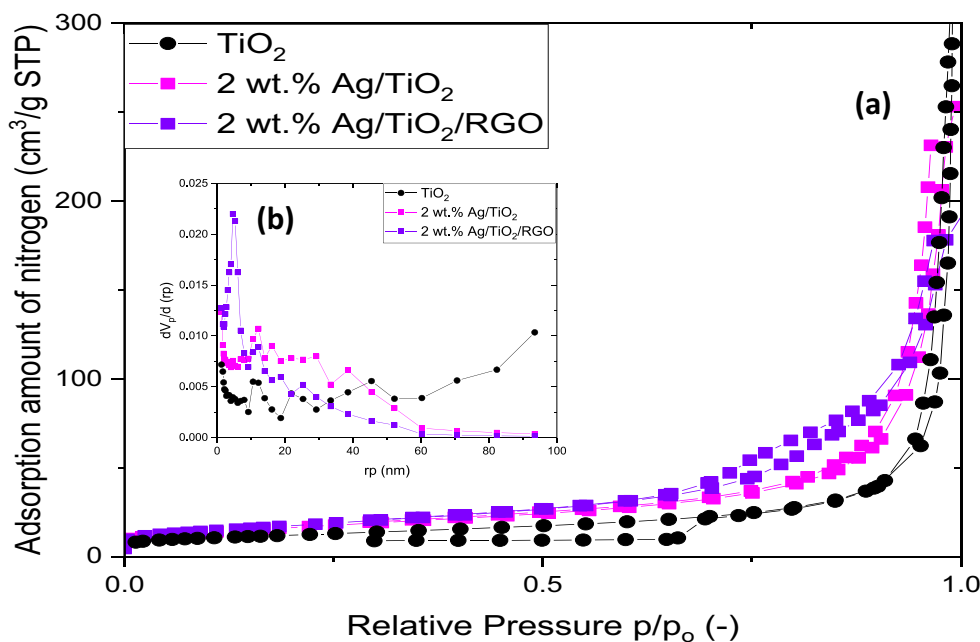


**Fig. 8** (a)  $N_2$  adsorption/desorption isotherms at 77 K for the as-prepared catalysts. (b) Pore size distribution curve



of all synthesized catalysts. It could be noticed that  $Ag$  NPs and graphene samples exhibit a red shift towards the visible region. As seen in Fig. 9a,  $Ag$  sample spectra show a surface plasmon resonance (SPR) which appeared as shoulder peaks in the range of visible light region (Wang et al. 2019; Tan et al. 2015). This is a further evidence of  $Ag$  NP existence as recognized by STEM, TEM, and EDX analysis. The SPR effect of  $Ag$  nanoparticles was clearly observed at 485 nm for  $Ag/TiO_2$  sample which is comparable to reported results by Hsu and Chen (2015). However, the incorporation of RGO could extend the absorption edge with a wide absorption broadband in the range of 400–800 nm which differs than the absorption band edge of  $Ag/TiO_2$  photocatalyst (Hou et al. 2019). The band gap energies were estimated using Kubelka-Munk function vs. the photon energy as depicted in Fig. 9b. It is well clear that the  $Ag$  doping and the addition of RGO sheets contribute to the decrease of the band gap energies of catalysts compared to  $TiO_2$  that was in agreement with previous studies (Vasilaki et al. 2015; Tahir and Amin 2017; Doluel et al. 2020). The reduction of the band gap energy in the ternary composite  $Ag/TiO_2/RGO$  could be attributed to the presence of Ti-O-C and/or Ti-C bonds between  $TiO_2$  and RGO as

reported in Akhavan and Ghaderi (2013), Hou et al. (2019), and El-Bery et al. (2017).

### Photoelectrochemical measurements

In order to examine the photoactivity of catalysts, photoelectrochemical measurements (PEC) were conducted in three-electrode cell immersed in 0.1 M  $Na_2SO_4$  electrolyte. Prior to measurements, argon gas purging was performed for 30 min. The linear sweep voltammetry (LSV) was carried out to determine the magnitude of electrodes photocurrent with numerous on/off cycles while chronoamperometry (CAM) was investigated to evaluate the photocurrent density and electrodes stability. Later, electrochemical impedance (EIS) was measured to determine the interfacial resistance and charge transfer capability. Meso-porous catalyst powders were deposited using the electrophoretic deposition (EPD) method without any post-treatment such as necking or heating.

Figure 10 shows the photocurrent-potential relationship under chopped UV-LED light with a wavelength of 365 nm and the average light intensity of 50  $mW/cm^2$ . The LSV at negative applied bias gives a positive photocurrent which

**Table 2** The surface area, pore volume, and the band gap energies of all samples

Sample	$N_2$ adsorption/desorption analysis		(DRS) analysis
	BET Surface area ( $m^2/g$ )	BJH adsorption pore volume ( $cm^3/g$ )	Band gap (eV)
$TiO_2$	46.66	0.4968	3.00
2 wt.% $Ag/TiO_2$	56.18	0.3868	2.78
2 wt.% $Ag/TiO_2/RGO$	61.37	0.2937	2.70

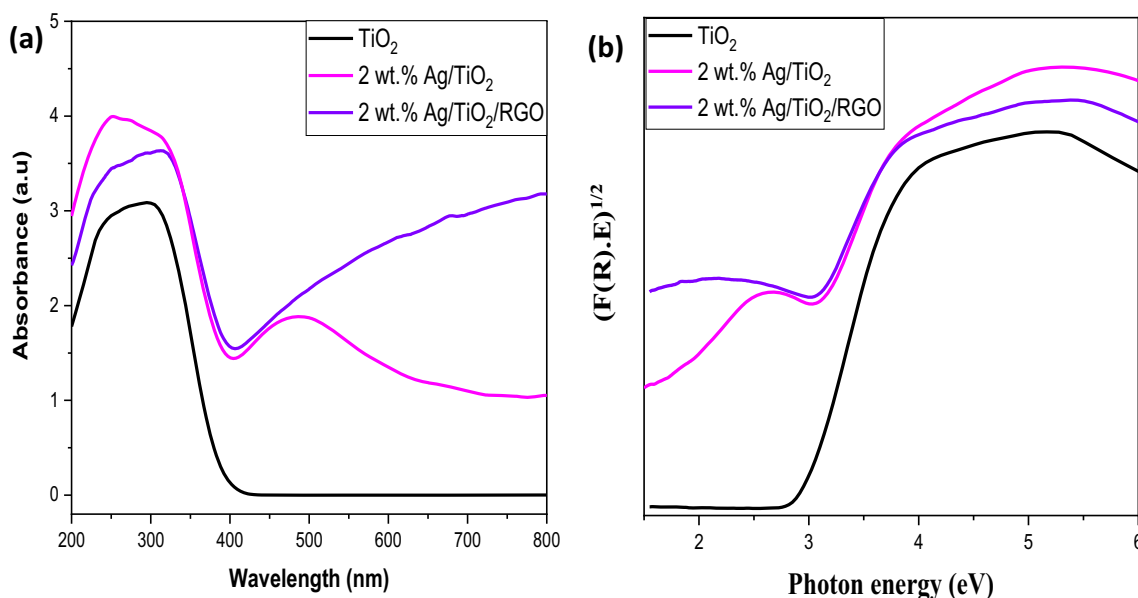


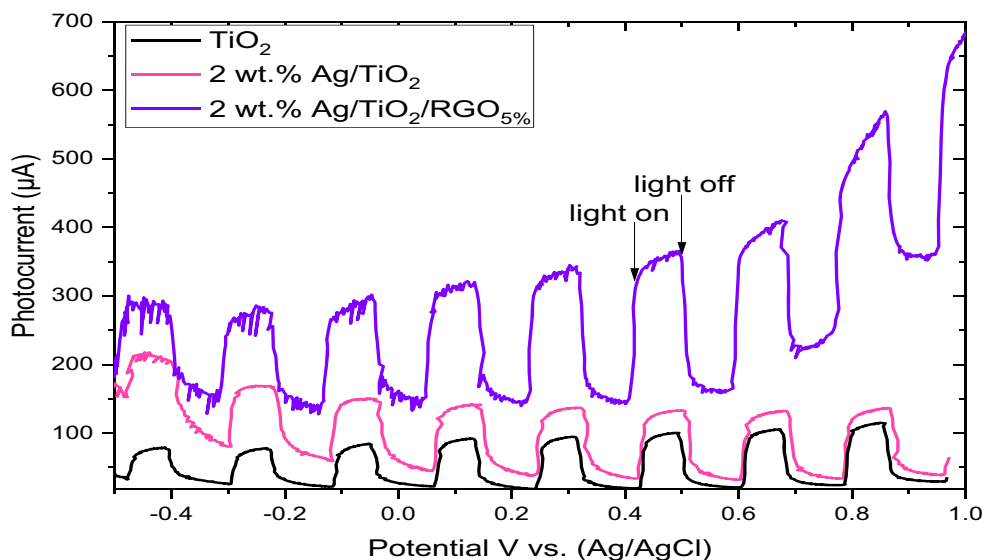
**Fig. 9** a UV-Vis diffuse reflectance spectra and b transformed Kubelka-Munk function vs. the photon energy for all samples

indicates the n-type behavior of catalysts. The reproducibility of the photocurrent generated confirms that all electrodes had an efficient response with instant illumination while the anodic photocurrent improved for those electrodes which contain Ag and RGO as shown in Fig. 10 compared with bare TiO<sub>2</sub> electrode. Furthermore, RGO substantially enhanced the photocatalytic performance, which could be attributed to its superior electrical conductivity. This facilitates the charge separation and reduces the recombination rate at interfaces and acts as sink of the photogenerated electrons (C. Wang et al. 2014; Sun et al. 2013; Meng et al. 2014; Meng et al. 2019). In addition, it was reported that under UV-irradiation photogenerated electrons of TiO<sub>2</sub> could reduce the remaining GO oxygenated function groups (sp<sup>2</sup> restoration) that exist in the photocatalysts composite. This could explain the

increment of the photocurrent with increasing potential and the time of irradiation in case of Ag/TiO<sub>2</sub>/RGO composite. The further deoxygenation of the partially reduced graphene oxide components under the photocatalytic reactions was considerably reported as in Williams et al. (2008) and Akhavan et al. (2010) with TiO<sub>2</sub> semiconductor, and with ZnO as a semiconductor in Williams and Kamat (2009) and Akhavan (2010). Moreover, electron trap and SPR occurred owing to the existence of Ag NPs that could lower the recombination of electron-hole pairs. Similar observations were reported in previous studies (Ahmed et al. 2018; Arif Sher Shah et al. 2013; Chaudhary et al. 2017).

To further assess the photoactivity of catalysts, Fig. 11 shows the chronoamperometry (at +0.6 vs. Ag/AgCl) for 800 s which included 60 s in dark before turning on light for

**Fig. 10** Photocurrent potential profiles (LSV) for all as-prepared catalysts under several on/off cycles



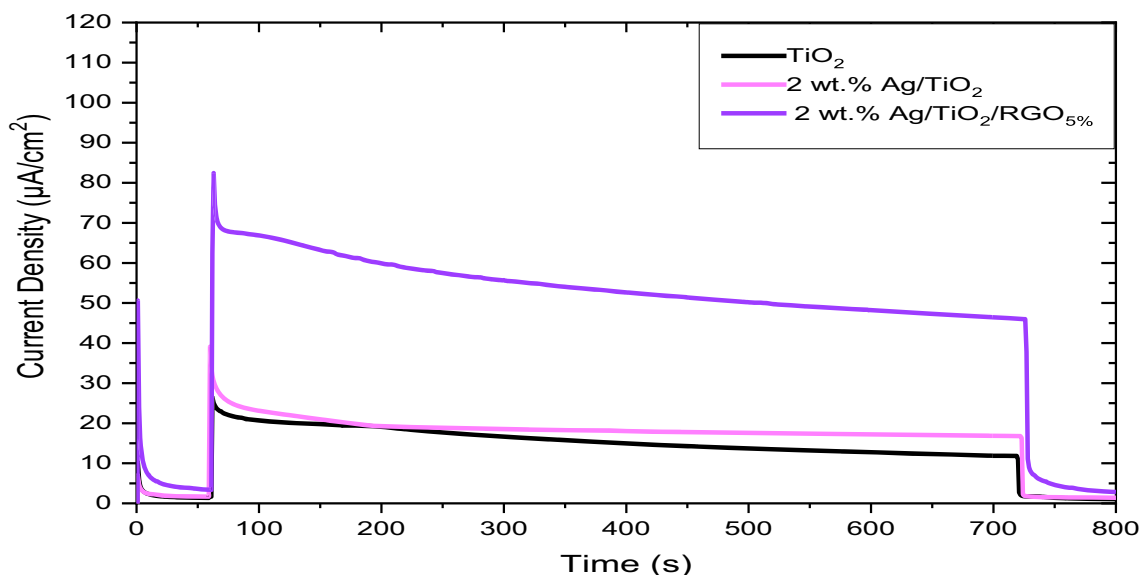


**Fig. 11** Transient photocurrent response (CAM) of synthesized catalysts at +0.6 vs. Ag/AgCl in 0.1 M Na<sub>2</sub>SO<sub>4</sub> electrolyte under UV LED light irradiation (365 nm)

600 s then turning off light once again until the completion of the measurement. It is well seen from the figure that all samples exhibit excellent photocurrent stability; however, the ternary composite of Ag/TiO<sub>2</sub>/RGO shows the superior activity compared with the binary composite of Ag/TiO<sub>2</sub> and bare TiO<sub>2</sub>. This confirms the results obtained in the previous section of LSV which may be assigned to the higher separation of electrons and less recombination of electron-hole pairs in the Ag/TiO<sub>2</sub>/RGO catalyst (Wang et al. 2019; Sang et al. 2019).

In order to test the charge transfer resistance of the prepared composites, EIS was recorded at dark and light conditions as depicted in Fig. 12 in 0.1 M Na<sub>2</sub>SO<sub>4</sub> solution at a frequency ranging from 100 kHz to 0.01 Hz and at 0.0 V (vs. Ag/AgCl).

In Fig. 12, the beginning section of the intercept between the circular arc in the Nyquist plot and real impedance ( $Z_{real}$ ) demonstrates the bulk electrolyte resistance ( $R_e$ ) or the equivalent series resistance (ESR) located at high-frequency region while the middle section of the arc exhibits the charge transfer resistance ( $R_{CT}$ ) located at the intermediate frequency. The smaller the arc diameter, the smaller the charge transfer resistance, and consequently effective charge transfer. This confirms the superior photocatalytic activity of the ternary composite of Ag/TiO<sub>2</sub>/RGO compared with Ag/TiO<sub>2</sub> and bare TiO<sub>2</sub> catalysts. The efficient separation of electrons which caused by both Ag and RGO incorporation is the reason of this enhanced activity of Ag/TiO<sub>2</sub>/RGO composite. Similar

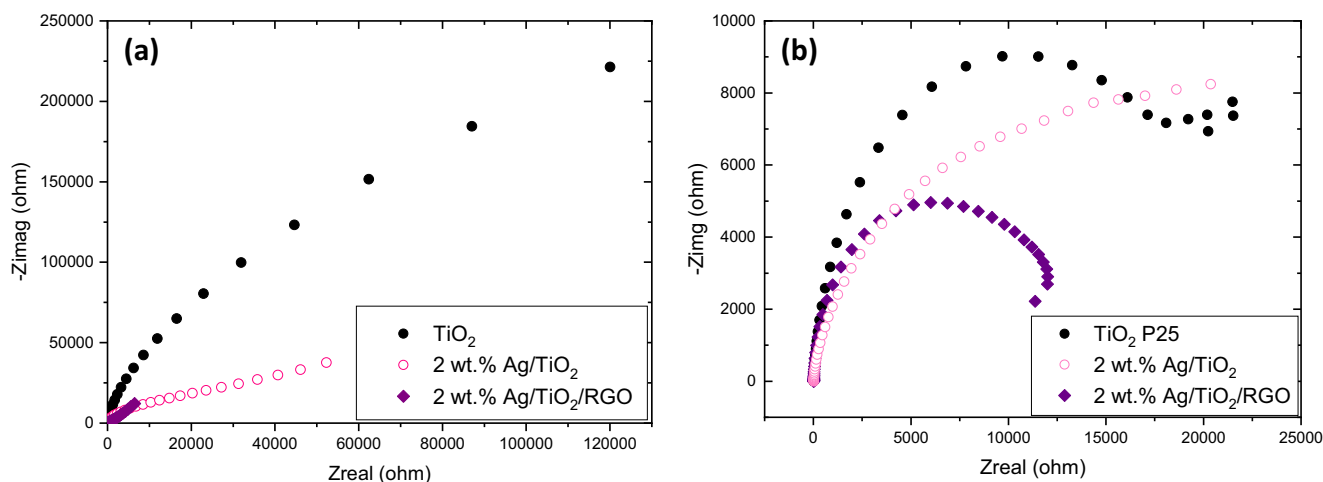


**Fig. 12** Nyquist plots of the EIS data for TiO<sub>2</sub>, 2 wt.% Ag/TiO<sub>2</sub>, 2 wt.% Ag/TiO<sub>2</sub>/RGO in 0.1 M Na<sub>2</sub>SO<sub>4</sub> electrolyte, under dark (a), and light irradiation ( $\lambda = 365$  nm) (b) at 0.0 V (vs. Ag/AgCl)

results were reported elsewhere (Chaudhary et al. 2017; Saquib et al. 2020).

### Photoconversion of CO<sub>2</sub> into organic compounds

The synthesized nanocomposites along with TiO<sub>2</sub>/RGO photocatalyst were further examined to reduce CO<sub>2</sub> in the presence of water into valuable organic compounds in the advanced meso-scale continuous-flow-type photochemical reactor cooperated with the proposed setup. Figure 13 shows the concentrations of both TOC and formaldehyde. TOC was analyzed using total organic carbon analyzer while formaldehyde was separately analyzed by Nash method. The proposed conditions used to reduce CO<sub>2</sub> were 30 mg of each photocatalyst weight, 30°C of the reactor temperature, 65 ml of water volume, and 500 µl/min for liquid pump flow rate which equals to 20 min of reactants' retention time inside the reactor.

In order to further identify the produced TOC, analysis on GC/MS was performed as displayed in Fig. 14. It is evident that the major product was methanol in the aqueous phase while the minor product was formaldehyde as seen in Figs. 13 and 14. In many applications, methanol is much preferable than gaseous products because it could be easily transported and stored. Previous findings confirmed that methanol was the main product in the photocatalytic reduction of CO<sub>2</sub> when water was used as a reductant and Ag/TiO<sub>2</sub> as a catalyst with different reactor configurations and setups (Yu et al. 2016; Liu et al. 2014; Kočí et al. 2011). It is well obvious that the use of

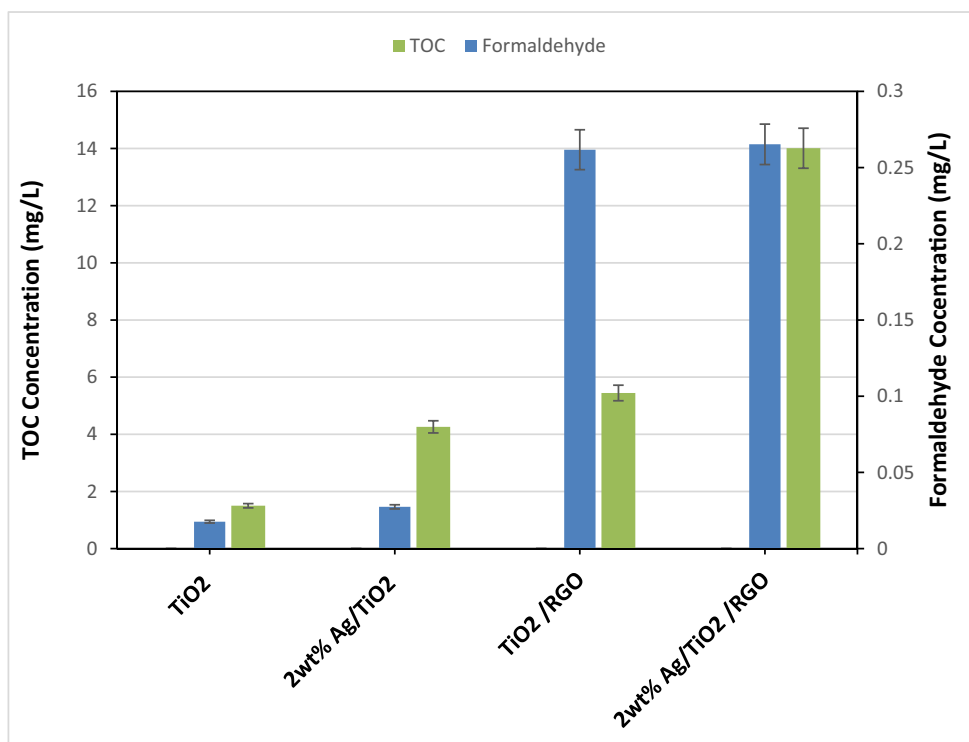
LED lamp to save energy as well as less catalyst utilization to produce methanol and other organic compounds in this setup emphasize the proficiency of this reactor compared with other previous setups used to reduce CO<sub>2</sub>. The formaldehyde concentration was too small as shown in Figs. 13 and 14 and the maximum concentration was achieved via Ag/TiO<sub>2</sub>/RGO which reached 0.26 mg/L.

In relation to catalysts, Ag/TiO<sub>2</sub>/RGO shows the superior photocatalytic activity towards TOC production that confirms results obtained from PEC measurements when the catalyst increases the photogenerated current compared with Ag/TiO<sub>2</sub> and bare TiO<sub>2</sub>. The photocatalytic activity of CO<sub>2</sub> reduction as well as photocurrent generation was found to be in the following sequence Ag/TiO<sub>2</sub>/RGO > Ag/TiO<sub>2</sub> > TiO<sub>2</sub>.

Comparing Ag/TiO<sub>2</sub> catalyst with bare TiO<sub>2</sub>, the enhancement of TOC productivity was assigned to Ag NP doping which act as electron trap to facilitate charge separation resulting in the increment of TOC production (Tan et al. 2015).

Moreover, the TiO<sub>2</sub>/RGO catalyst was examined in CO<sub>2</sub> photocatalytic reduction as shown in Fig. 13 to further identify the effectiveness of the incorporation of RGO together with TiO<sub>2</sub> semiconductor. Its result showed that a little improvement of organic carbon production (TOC) was achieved in comparison with Ag/TiO<sub>2</sub> photocatalyst. However, the amount of formaldehyde produced in this case exceeded the produced amount of formaldehyde in case of Ag/TiO<sub>2</sub>. It was reported that the exfoliated graphene has an effective surface area ~2600 m<sup>2</sup>/g which promotes the traveling of electrons without

**Fig. 13** Dependence of product concentrations on photocatalysts type in certain conditions (weight of catalyst = 30 mg, volume of deionized water = 65 ml, retention time = 20 min, and reactor temperature = 30°C)



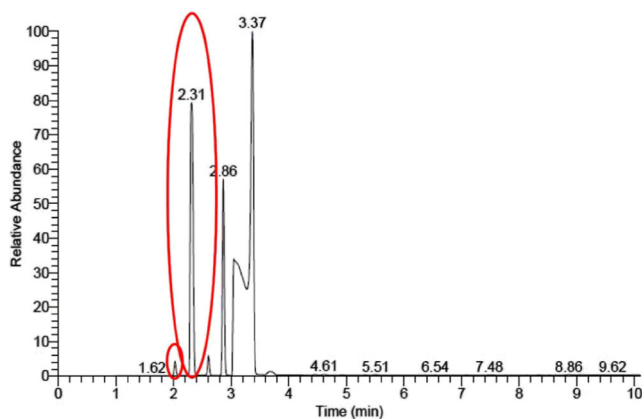


**Fig. 14** The chromatographic peak on GC/MS corresponding to methanol at 2.31 min and formaldehyde peak at 2.14 min. (the peak at 2.86 min belonged to acetone due to syringe washing while the peak at 3.37 min was for methylene chloride from extraction)

scattering at mobility up to  $\sim 15,000 \text{ m}^2/\text{V} \cdot \text{s}$  at room temperature. Obviously, graphene plays an essential role and acts as electrons sink or electrons bridge (Jeyalakshmi et al. 2012).

The use of graphene in the Ag/TiO<sub>2</sub>/RGO ternary composite enhanced the photocatalytic reduction of CO<sub>2</sub> by 3.3 and 9.4 times compared with Ag/TiO<sub>2</sub> and bare TiO<sub>2</sub>, respectively, using the proposed photochemical reactor in a continuous mode. The reason why Ag/TiO<sub>2</sub>/RGO has a superior photocatalytic activity over other catalysts is that RGO facilitates the mobility of the photoexcited electrons prior to be trapped by Ag NPs that consequently decreases the recombination of electron-hole pairs.

Comparing the results of the ternary composite of Ag/TiO<sub>2</sub>/RGO with the binary composite of TiO<sub>2</sub>/RGO, no change was found in the amount of formaldehyde while the methanol concentration was significantly increased by 2.6-fold as verified by TOC analysis. This confirms the synergistic effect of Ag NPs and RGO along with TiO<sub>2</sub> as the main reason for improving the photocatalytic conversion of CO<sub>2</sub> into methanol as the major product.

## Proposed mechanism of CO<sub>2</sub> photocatalytic reduction

The reduction of CO<sub>2</sub> with water takes place according to Eqs. (6)–(12) and illustrated in Fig. 15 (Habisreutinger et al. 2013; Ran et al. 2018; Hiragond et al. 2019; Chang et al. 2016). The process begins with semiconductor excitation to produce electron-hole pairs. Later, holes are consumed to oxidize water molecules to form hydrogen ions (H<sup>+</sup>) and hydroxyl radicals (OH<sup>•</sup>) which further be react with holes to produce oxygen while electrons reduce the adsorbed CO<sub>2</sub> on the surface of the semiconductor to form methanol and other valuable hydrocarbons. The RGO existence provides a fast mobility for electrons to facilitate separation then Ag enhance the

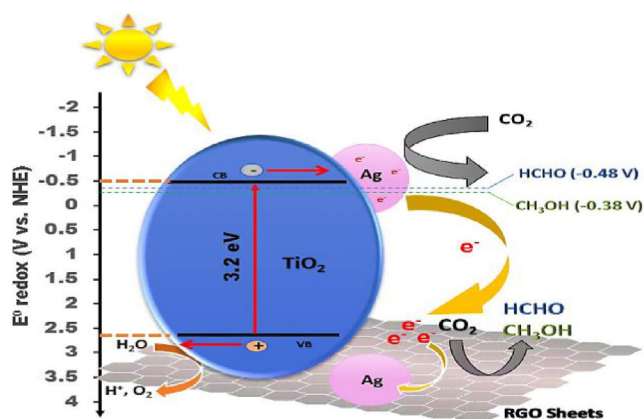
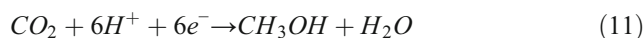
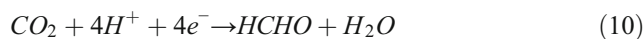
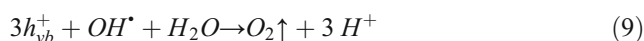


**Fig. 15** Proposed mechanism of the photocatalytic reduction of CO<sub>2</sub> over Ag/TiO<sub>2</sub> and Ag/TiO<sub>2</sub>/RGO composites and energy band gap position vs. NHE

separation process via trapping of those electrons to further be utilized in CO<sub>2</sub> reduction and consequently produce higher carbon compounds such as formaldehyde and methanol as illustrated in Eqs. (10, 11). The last equation (Eq. (12)) exhibits the competitive reaction of reducing hydrogen instead of CO<sub>2</sub>. In this case of using the advanced meso-scale continuous-flow type photochemical reactor, the GC analysis confirms that the reactor suppresses the formation of hydrogen and induces the reduction of CO<sub>2</sub>.



## Conclusion

The advanced meso-scale continuous-flow-type photochemical reactor exhibits an outstanding performance towards CO<sub>2</sub> photocatalytic reduction with liquid water. GC results confirm that the reactor suppresses the production of H<sub>2</sub>, the competitive reaction, which enhances the reduction of CO<sub>2</sub> and consequently the production of various valuable hydrocarbons via consuming less amount of catalysts.

The use of graphene increases the TOC production by 3.3 and 9.4 times compared with Ag/TiO<sub>2</sub> and bare TiO<sub>2</sub>,

respectively, using the proposed photochemical reactor in a continuous mode.

**Acknowledgements** The first author is grateful to the Egypt-Japan University of Science and Technology (E-JUST), especially Prof. Dr. Ahmed H. El-Shazly, for providing the support and supervision to complete this work.

**Author contribution** All authors contributed to the study conception and design. Material preparation, data collection, and analysis were performed by Samar Nabil, Ahmed Hammad, and Haitham El-Bery. The supervision, discussion of results, and suggestion of the research point were performed by prof. Elsayed A. Shalaby and prof. Ahmed H. El-Shazly. The first draft of the manuscript was written by Samar Nabil and all authors commented on previous versions of the manuscript. All authors read and approved the final manuscript.

**Funding** The analysis of all samples as well as all experiments was conducted in the laboratories of Egypt-Japan University of Science and Technology (E-JUST).

**Availability of data and materials** All data generated or analyzed during this study are included in this published article.

## Declarations

**Ethics approval and consent to participate** The manuscript does not involve the use of any animal or human data or tissue.

**Consent for publication** The manuscript does not contain data from any individual person.

**Competing interests** The authors declare no competing interests.

## References

- Abrishamkar M, Barootkoob M (2017) Electrooxidation of formaldehyde as a fuel for fuel cells using Fe<sup>2+</sup>-nano-zeolite modified carbon paste electrode. *Int J Hydrog Energy* 42(37):23821–23825. <https://doi.org/10.1016/j.ijhydene.2017.04.083>
- Ahmed N, Ramadan M, El Roubay WMA, Farghali AA, Allam NK (2018) Non-precious co-catalysts boost the performance of TiO<sub>2</sub> hierarchical hollow mesoporous spheres in solar fuel cells. *Int J Hydrog Energy* 43:21219–21230. <https://doi.org/10.1016/j.ijhydene.2018.10.012>
- Akhavan O (2010) Graphene nanomesh by ZnO nanorod photocatalysts. *ACS Nano* 4(7):4174–4180. <https://doi.org/10.1021/nn1007429>
- Akhavan O, Ghaderi E (2009) Photocatalytic reduction of graphene oxide nanosheets on TiO<sub>2</sub> thin film for photoinactivation of bacteria in solar light irradiation. *J Phys Chem C* 113(47):20214–20220. <https://doi.org/10.1021/jp906325q>
- Akhavan O, Ghaderi E (2013) Flash photo stimulation of human neural stem cells on graphene/TiO<sub>2</sub> heterojunction for differentiation into neurons. *Nanoscale* 5(21):10316–10326. <https://doi.org/10.1039/c3nr02161k>
- Akhavan O, Abdolohad M, Esfandiari A, Mohatahshamifard M (2010) Photodegradation of graphene oxide sheets by TiO<sub>2</sub> nanoparticles after a photocatalytic reduction. *J Phys Chem C* 114(30):12955–12959. <https://doi.org/10.1021/jp103472c>
- Arif Sher Shah MS, Zhang K, Park AR, Kim KS, Park NG, Park JH, Yoo PJ (2013) Single-step solvothermal synthesis of mesoporous Ag-TiO<sub>2</sub>-reduced graphene oxide ternary composites with enhanced photocatalytic activity. *Nanoscale* 5(11):5093–5101. <https://doi.org/10.1039/c3nr00579h>
- Chang X, Zheng J (2015) Photocatalytic conversion of CO<sub>2</sub> into value-added hydrocarbon (methanol) with high selectivity over ZnS nanoparticles driven by 355-nm pulsed laser. *Res Chem Intermed* 41:739–747. <https://doi.org/10.1007/s11164-013-1224-y>
- Chang X, Wang T, Gong J (2016) CO<sub>2</sub> photo-reduction: insights into CO<sub>2</sub> activation and reaction on surfaces of photocatalysts. *Energy Environ Sci* 9(7):2177–2196. <https://doi.org/10.1039/C6EE00383D>
- Chaudhary D, Singh S, Vankar VD, Khare N (2017) A ternary Ag/TiO<sub>2</sub>/CNT photoanode for efficient photoelectrochemical water splitting under visible light irradiation. *Int J Hydrog Energy* 42(12):7826–7835. <https://doi.org/10.1016/j.ijhydene.2016.12.036>
- Chen W-Y, Shi GK, Hailey A, Tsai EST, Hammer N, Wu Z (2012) Photocatalytic conversion of carbon dioxide to organic compounds using a green photocatalyst: an undergraduate research experiment. *Chem Educ* 17(4):166–172. <https://doi.org/10.1007/s00897122438>
- Crake A, Christoforidis KC, Kafizas A, Zafeirotas S, Petit C (2017) CO<sub>2</sub> capture and photocatalytic reduction using bifunctional TiO<sub>2</sub>/MOF nanocomposites under UV-vis irradiation. *Appl Catal B Environ* 210:131–140. <https://doi.org/10.1016/j.apcatb.2017.03.039>
- Doluel EC, Kartal U, Dikici T, Yurddaskal M (2020) Effect of Ag content on photocatalytic activity of Ag@TiO<sub>2</sub>/rGO hybrid photocatalysts. *J Electron Mater* 49(6):3849–3859. <https://doi.org/10.1007/s11664-020-08102-0>
- Dong WH, Wu DD, Luo JM, Xing QJ, Liu H, Zou JP, Luo XB, Min XB, Liu HL, Luo SL, Au CT (2017) Coupling of photodegradation of RhB with photoreduction of CO<sub>2</sub> over rGO/SrTi<sub>0.95</sub>Fe<sub>0.05</sub>O<sub>3</sub>-Δ catalyst: a strategy for one-pot conversion of organic pollutants to methanol and ethanol. *J Catal* 349:218–225. <https://doi.org/10.1016/j.jcat.2017.02.004>
- El-Bery HM, Matsushita Y, Abdel-moneim A (2017) Fabrication of efficient TiO<sub>2</sub>-RGO heterojunction composites for hydrogen generation via water-splitting: comparison between RGO, Au and Pt reduction sites. *Appl Surf Sci* 423:185–196. <https://doi.org/10.1016/j.apsusc.2017.06.130>
- Feng X, Pan F, Tran BZ, Li Y (2020) Photocatalytic CO<sub>2</sub> reduction on porous TiO<sub>2</sub> synergistically promoted by atomic layer deposited MgO overcoating and photodeposited silver nanoparticles. *Catal Today* 339(October 2018):328–336. <https://doi.org/10.1016/j.cattod.2019.03.012>
- Gui MM, Wong WMP, Chai SP, Mohamed AR (2015) One-pot synthesis of Ag-MWCNT@TiO<sub>2</sub> core-shell nanocomposites for photocatalytic reduction of CO<sub>2</sub> with water under visible light irradiation. *Chem Eng J* 278:272–278. <https://doi.org/10.1016/j.cej.2014.09.022>
- Habisreutinger SN, Schmidt-Mende L, Stolarczyk JK (2013) Photocatalytic reduction of CO<sub>2</sub> on TiO<sub>2</sub> and other semiconductors. *Angew Chem Int Ed* 52(29):7372–7408. <https://doi.org/10.1002/anie.201207199>
- Heggo D, Mohamed H, Ookawara S, Matsushita Y (2016) Process intensification of photocatalytic p-anisaldehyde synthesis by using mini batch reactor and UV-LED. *J Chem Eng Jpn* 49(2):130–135. <https://doi.org/10.1252/jcej.15we042>
- Hiragond C, Ali S, Sorcar S, In SI (2019) Hierarchical nanostructured photocatalysts for CO<sub>2</sub> photoreduction. *Catalysts* 9(4):370. <https://doi.org/10.3390/catal9040370>
- Hou Y, Pu S, Shi Q, Mandal S, Ma H, Xue S, Cai G, Bai Y (2019) Ultrasonic impregnation assisted in-situ photoreduction deposition synthesis of Ag/TiO<sub>2</sub>/rGO ternary composites with synergistic enhanced photocatalytic activity. *J Taiwan Inst Chem Eng* 104:139–150. <https://doi.org/10.1016/j.jtice.2019.08.023>

- Hsu KC, Chen DH (2015) Highly sensitive, uniform, and reusable surface-enhanced raman scattering substrate with TiO<sub>2</sub> interlayer between Ag nanoparticles and reduced graphene oxide. *ACS Appl Mater Interfaces* 7(49):27571–27579. <https://doi.org/10.1021/acsami.5b08792>
- Jeyalakshmi V, Mahalakshmy R, Krishnamurthy KR, Viswanathan B (2012) Titania based catalysts for photoreduction of carbon dioxide: role of modifiers. *Indian J Chem - Section A Inorgan, Physical, Theor Anal Chem* 51(9–10):1263–1283
- Josland S, Mumtaz S, Oelgemöller M (2016) Photodecarboxylations in an advanced meso-scale continuous-flow photoreactor. *Chem Eng Technol* 39(1):81–87. <https://doi.org/10.1002/ceat.201500285>
- Karamian E, Sharifnia S (2016) On the general mechanism of photocatalytic reduction of CO<sub>2</sub>. *J CO<sub>2</sub> Util* 16:194–203. <https://doi.org/10.1016/j.jcou.2016.07.004>
- Kočí K, Matějů K, Obalová L, Krejčíková S, Lacný Z, Plachá D, Čapek L, Hospodková A, Šolcová O (2010) Effect of silver doping on the TiO<sub>2</sub> for photocatalytic reduction of CO<sub>2</sub>. *Appl Catal B Environ* 96(3–4):239–244. <https://doi.org/10.1016/j.apcatb.2010.02.030>
- Kočí K, Zatloukalová K, Obalová L, Krejčíková S, Lacný Z, Čapek L, Hospodková A, Šolcová O (2011) Wavelength effect on photocatalytic reduction of CO<sub>2</sub> by Ag/TiO<sub>2</sub> catalyst. *Cuihua Xuebao/Chin J Catal* 32(5):812–815. [https://doi.org/10.1016/s1872-2067\(10\)60199-4](https://doi.org/10.1016/s1872-2067(10)60199-4)
- Kometani N, Hirata S, Chikada M (2017) Photocatalytic reduction of CO<sub>2</sub> by Pt-loaded TiO<sub>2</sub> in the mixture of sub- and supercritical water and CO<sub>2</sub>. *J Supercrit Fluids* 120:443–447. <https://doi.org/10.1016/j.supflu.2016.05.031>
- Li J, Zeng X, Ren T, van der Heide E (2014) The preparation of graphene oxide and its derivatives and their application in bio-tribological systems. *Lubricants* 2(3):137–161. <https://doi.org/10.3390/lubricants2030137>
- Liu E, Kang L, Wu F, Sun T, Hu X, Yang Y, Liu H, Fan J (2014) Photocatalytic reduction of CO<sub>2</sub> into methanol over Ag/TiO<sub>2</sub> nanocomposites enhanced by surface plasmon resonance. *Plasmonics* 9(1):61–70. <https://doi.org/10.1007/s11468-013-9598-7>
- Liu L, Zhang Y, Zhang B, Feng Y (2017) A detailed investigation on the performance of dye-sensitized solar cells based on reduced graphene oxide-doped TiO<sub>2</sub> photoanode. *J Mater Sci* 52(13):8070–8083. <https://doi.org/10.1007/s10853-017-1014-9>
- Liu X, Xu T, Li Y, Zang Z, Peng X, Wei H, Zha W, Wang F (2018) Enhanced X-ray photon response in solution-synthesized CsPbBr<sub>3</sub> nanoparticles wrapped by reduced graphene oxide. *Sol Energy Mater Sol Cells* 187(August):249–254. <https://doi.org/10.1016/j.solmat.2018.08.009>
- Loubière K, Oelgemöller M, Aillet T, Dechy-cabaret O, Prat L (2016) Continuous-flow photochemistry: a need for chemical engineering. *Chem Eng Process Process Intensif* 104:120–132. <https://doi.org/10.1016/j.cep.2016.02.008>
- Low J, Cheng B, Yu J (2017) Surface modification and enhanced photocatalytic CO<sub>2</sub> reduction performance of TiO<sub>2</sub>: a review. *Appl Surf Sci* 392:658–686. <https://doi.org/10.1016/j.apsusc.2016.09.093>
- Meng D, Yang S, Guo L, Li G, Ge J, Huang Y, Bielawski CW, Geng J (2014) The enhanced photothermal effect of graphene/conjugated polymer composites: photoinduced energy transfer and applications in photocontrolled switches. *Chem Commun* 50(92):14345–14348. <https://doi.org/10.1039/c4cc06849a>
- Meng D, Fan J, Ma J, Du SW, Geng J (2019) The preparation and functional applications of carbon nanomaterial/conjugated polymer composites. *Compos Commun* 12(December 2018):64–73. <https://doi.org/10.1016/j.coco.2018.12.009>
- Naraginti S, Yong YC (2019) Enhanced detoxification of p-bromophenol by novel Zr/Ag-TiO<sub>2</sub>@rGO ternary composite: degradation kinetics and phytotoxicity evolution studies. *Ecotoxicol Environ Saf* 170(December 2018):355–362. <https://doi.org/10.1016/j.ecoenv.2018.12.001>
- Nash T (1953) The colorimetric estimation of formaldehyde by means of the Hantzsch reaction. *Biochem J* 55(3):416–421. <https://doi.org/10.1042/bj0550416>
- Némethné-Sóvágó J, Benke M (2014) Microreactors: a new concept for chemical synthesis and technological feasibility. *Mater Sci Eng* 39(2):89–101
- Ola O, Maroto-Valer MM (2015) Review of material design and reactor engineering on TiO<sub>2</sub> photocatalysis for CO<sub>2</sub> reduction. *J Photochem Photobiol C: Photochem Rev* 24:16–42. <https://doi.org/10.1016/j.jphotochemrev.2015.06.001>
- Rajalakshmi K, Jeyalakshmi V, Krishnamurthy KR, Viswanathan B (2012) Photocatalytic reduction of carbon dioxide by water on titania: role of photophysical and structural properties. *Indian J Chem - Section A Inorgan, Physical, Theor Anal Chem* 51(3):411–419
- Ran J, Jaroniec M, Qiao SZ (2018) Cocatalysts in semiconductor-based photocatalytic CO<sub>2</sub> reduction: achievements, challenges, and opportunities. *Adv Mater* 30(7):1–31. <https://doi.org/10.1002/adma.201704649>
- Sang L, Lei L, Burda C (2019) Electrochemical fabrication of rGO-embedded Ag-TiO<sub>2</sub> nanoring/nanotube arrays for plasmonic solar water splitting. *Nano-Micro Lett* 11(1):1–16. <https://doi.org/10.1007/s40820-019-0329-2>
- Saqib M, Kaushik R, Halder A (2020) Photoelectrochemical Activity of Ag coated 2D-TiO<sub>2</sub>/RGO heterojunction for hydrogen evolution reaction and environmental remediation. *Chem Select* 5(21):6376–6388. <https://doi.org/10.1002/slct.202000843>
- Sellaro M, Bellardita M, Brunetti A, Fontananova E, Palmisano L, Drioli E, Barbieri G (2016) CO<sub>2</sub> conversion in a photocatalytic continuous membrane reactor. *RSC Adv* 6(71):67418–67427. <https://doi.org/10.1039/c6ra06777h>
- Shehzad N, Tahir M, Johari K, Murugesan T, Hussain M (2018) A critical review on TiO<sub>2</sub> based photocatalytic CO<sub>2</sub> reduction system: strategies to improve efficiency. *J CO<sub>2</sub> Util* 26(May):98–122. <https://doi.org/10.1016/j.jcou.2018.04.026>
- Sneddon G, Greenaway A, Yiu HHP (2014) The potential applications of nanoporous materials for the adsorption, separation, and catalytic conversion of carbon dioxide. *Adv Energy Mater* 4(10):1–19. <https://doi.org/10.1002/aenm.201301873>
- Spurr RA, Myers H (1957) Quantitative analysis of anatase-rutile mixtures with an X-ray diffractometer. *Anal Chem* 29(5):760–762. <https://doi.org/10.1021/ac60125a006>
- Sun J, Xiao L, Meng D, Geng J, Huang Y (2013) Enhanced photoresponse of large-sized photoactive graphene composite films based on water-soluble conjugated polymers. *Chem Commun* 49(49):5538–5540. <https://doi.org/10.1039/c3cc40563j>
- Tahir M, Amin NS (2013) Photocatalytic CO<sub>2</sub> reduction and kinetic study over In/TiO<sub>2</sub> nanoparticles supported microchannel monolith photoreactor. *Appl Catal A Gen* 467:483–496. <https://doi.org/10.1016/j.apcata.2013.07.056>
- Tahir M, Amin NAS (2017) Photo-induced CO<sub>2</sub> reduction by hydrogen for selective CO evolution in a dynamic monolith photoreactor loaded with Ag-modified TiO<sub>2</sub> nanocatalyst. *Int J Hydrog Energy* 42(23):15507–15522. <https://doi.org/10.1016/j.ijhydene.2017.05.039>
- Tahir B, Tahir M, Amin NS (2015) Performance analysis of monolith photoreactor for CO<sub>2</sub> reduction with H<sub>2</sub>. *Energy Convers Manag* 90:272–281. <https://doi.org/10.1016/j.enconman.2014.11.018>
- Tan LL, Ong WJ, Chai SP, Mohamed AR (2015) Noble metal modified reduced graphene oxide/TiO<sub>2</sub> ternary nanostructures for efficient visible-light-driven photoreduction of carbon dioxide into methane. *Appl Catal B Environ* 166–167:251–259. <https://doi.org/10.1016/j.apcatb.2014.11.035>
- Vasilaki E, Georgaki I, Vemardou D, Vamvakaki M, Katsarakis N (2015) Ag-loaded TiO<sub>2</sub>/reduced graphene oxide nanocomposites for enhanced visible-light photocatalytic activity. *Appl Surf Sci* 353:865–872. <https://doi.org/10.1016/j.apsusc.2015.07.056>



- Verhelst S, Turner JW, Sileghem L, Vancoillie J (2019) Methanol as a fuel for internal combustion engines. *Prog Energy Combust Sci* 70: 43–88. <https://doi.org/10.1016/j.pecs.2018.10.001>
- Wang P, Tang Y, Dong Z, Chen Z, Lim TT (2013) Ag-AgBr/TiO<sub>2</sub>/RGO nanocomposite for visible-light photocatalytic degradation of penicillin G. *J Mater Chem A* 1(15):4718–4727. <https://doi.org/10.1039/c3ta01042b>
- Wang C, Meng D, Sun J, Memon J, Huang Y, Geng J (2014) Graphene wrapped TiO<sub>2</sub> based catalysts with enhanced photocatalytic activity. *Adv Mater Interfaces* 1(4):1–8. <https://doi.org/10.1002/admi.201300150>
- Wang B, Chen W, Song Y, Li G, Wei W, Fang J, Sun Y (2018) Recent progress in the photocatalytic reduction of aqueous carbon dioxide. *Catal Today* 311(October):23–39. <https://doi.org/10.1016/j.cattod.2017.10.006>
- Wang Y, Zhang M, Fang L, Yang H, Zuo Y, Gao J, He G, Sun Z (2019) A multifunctional Ag/TiO<sub>2</sub>/reduced graphene oxide with optimal surface-enhanced Raman scattering and photocatalysis. *J Am Ceram Soc* 102(7):4000–4013. <https://doi.org/10.1111/jace.16273>
- Wei J, Zang Z, Zhang Y, Wang M, Du J, Tang X (2017) Enhanced performance of light-controlled conductive switching in hybrid cuprous oxide/reduced graphene oxide (Cu<sub>2</sub>O/rGO) nanocomposites. *Opt Lett* 42(5):911–914. <https://doi.org/10.1364/ol.42.000911>
- Williams G, Kamat PV (2009) Graphene-semiconductor nanocomposites: excited-state interactions between ZnO nanoparticles and graphene oxide. *Langmuir* 25(24):13869–13873. <https://doi.org/10.1021/la900905h>
- Williams G, Seger B, Kamat PV (2008) TiO<sub>2</sub>-graphene nanocomposites. UV-assisted photocatalytic reduction of graphene oxide. *ACS Nano* 2(7):1487–1491. <https://doi.org/10.1021/nm800251f>
- Wu J, Huang Y, Ye W, Li Y (2017) CO<sub>2</sub> reduction: from the electrochemical to photochemical approach. *Adv Sci* 4(11):1–29. <https://doi.org/10.1002/advs.201700194>
- Yang X, Xiao T, Edwards PP (2011) The use of products from CO<sub>2</sub> photoreduction for improvement of hydrogen evolution in water splitting. *Int J Hydrog Energy* 36(11):6546–6552. <https://doi.org/10.1016/j.ijhydene.2011.02.116>
- Yu B, Zhou Y, Li P, Tu W, Li P, Tang L, Ye J, Zou Z (2016) Photocatalytic reduction of CO<sub>2</sub> over Ag/TiO<sub>2</sub> nanocomposites prepared with a simple and rapid silver mirror method. *Nanoscale* 8(23):11870–11874. <https://doi.org/10.1039/c6nr02547a>
- Zang Z, Zeng X, Wang M, Hu W, Liu C, Tang X (2017) Tunable photoluminescence of water-soluble AgInZnS-graphene oxide (GO) nanocomposites and their application in-vivo bioimaging. *Sensors Actuators B Chem* 252:1179–1186. <https://doi.org/10.1016/j.snb.2017.07.144>

**Publisher's note** Springer Nature remains neutral with regard to jurisdictional claims in published maps and institutional affiliations.